

Tunable Majorana corner states driven by superconducting phase bias in a vertical Josephson junction

Cheng-Ming Miao,^{1,*} Yu-Hao Wan,^{1,*} Ying-Tao Zhang,² and Qing-Feng Sun^{1,3,†}

¹*International Center for Quantum Materials, School of Physics, Peking University, Beijing 100871, China*

²*College of Physics, Hebei Normal University, Shijiazhuang 050024, China*

³*Hefei National Laboratory, Hefei 230088, China*

The realization and manipulation of Majorana zero modes is a key step in achieving topological quantum computation. In this paper, we demonstrate the existence of Majorana corner states in a superconductor-insulators-superconductor vertical Josephson junction. The position of these Majorana corner states can be precisely and easily controlled by the superconducting phase bias, which be confirmed through both numerical and edge state theoretical analysis. In addition, we propose a protocol for achieving topological braiding of the Majorana corner states in a system of three circular vertical Josephson junctions. Our findings advance the field of topological quantum computation by providing new insights into the efficient and precise manipulation of Majorana corner states.

I. INTRODUCTION

Majorana zero modes are exotic quasiparticles that emerge as zero-energy solutions in the Majorana equation [1]. They obey non-Abelian exchange statistics and resist local perturbations, making them promising for topological quantum computation [2–11]. In condensed matter physics, Majorana zero modes are predicted to appear at boundaries or defects of topological superconductors (SCs), with platforms such as quantum wires [12–20], superconducting vortices [21–25], Josephson junctions [26–32], and SC-proximitized topological insulators or quantum anomalous Hall insulators (QAHIs) [33–37]. Observing their exchange statistics is crucial for topological braiding. To this end, various manipulation approaches have been proposed including electrostatically tuned gate voltages [38–42], strain-induced state density variation [43, 44], and probe-mediated vortex movement [45, 46]. Furthermore, two-dimensional second-order topological SCs host Majorana corner states (MCSs), special Majorana zero modes, offering inherent advantages for braiding [47–56]. Unlike Majorana zero modes in rigorous one-dimensional systems, MCSs can be exchanged without mixing, simplifying the braiding process. Based on this, several braiding schemes have been proposed including in-plane magnetic field tuning [57–61], LC-circuit emulation [62], electrically controlled chemical potentials [63], among others. Magnetic-field-based approaches [57–61] face significant challenges due to their reliance on high-precision magnetic fields (and sometimes simultaneous phase control) leads to imprecise operations or complex implementation. Meanwhile, existing magnetic-field-free methods [62, 63] exhibit their own limitations, such as limited mobility and flexibility of Majorana zero modes hinder efficient and continuous braiding operations [62], as well as sensitivity to edge ge-

ometry and imperfections may disturb the braiding evolution [63]. Building upon these insights, our work aims to develop a manipulation scheme that is efficient, precise, continuous, robust, and easily implementable. Notably, overcoming these challenges will make a significant contribution to the realization of topological quantum computing.

In this paper, we propose a scheme for manipulating MCSs by superconducting phase bias in an SC-middle insulators-SC vertical Josephson junction without a magnetic field. Specifically, the middle insulators are structured as a QAH-normal insulator (NI)-QAH sandwich structure, and the superconducting phase bias can be controlled by a supercurrent [see Figs. 1(a,b)]. It is demonstrated that superconducting phase bias can effectively manipulate the position of MCSs. The emergence and movement of these MCSs can be explained by the edge states orthogonal theory. In addition, we propose a topological braiding protocol by exchanging the positions of MCSs in a hybrid system of three circular vertical Josephson junctions (CVJJs). Our findings advance topological quantum computation by offering new insights into the efficient, precise, continuous, robust, and easy manipulation of MCSs by superconducting phase bias.

The paper is structured as follows. In Sec. II, we present the model Hamiltonian for the CVJJs. Section III demonstrates the emergence of MCSs and shows that two such MCSs can be efficiently and easily manipulated by tuning the superconducting phase bias. In Sec. IV, we elaborate on the origin of MCSs, and prove that their positions can be precisely and continuously controlled based on numerical and analytical results. Then in Sec. V, we propose a protocol for achieving the topological braiding by swapping two of the four MCSs. Finally, a summary is presented in Sec. VI. Some auxiliary materials are relegated to Appendices A to C.

* These authors contribute equally to this work.

† sunqf@pku.edu.cn

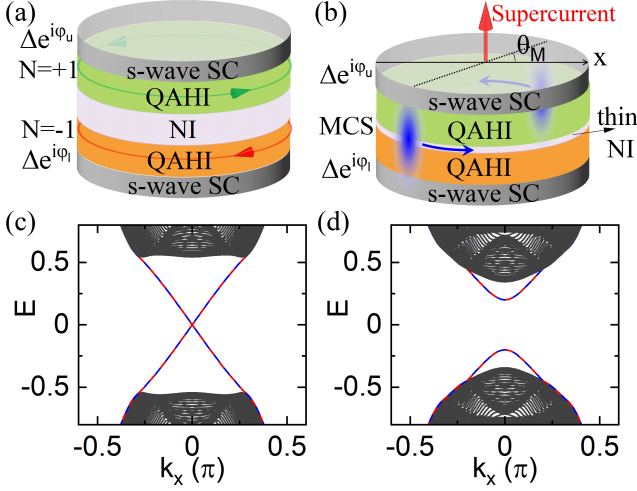


FIG. 1. (a,b) Schematic of the SC/QAHI/Ni/QAHI/SC vertical Josephson junction. The green and orange QAHI hosts opposite Chern numbers. Δ and $\varphi_{u(l)}$ represent the superconducting pairing potential and phase of the grey *s*-wave SC. (a) Majorana edge states propagate counterclockwise/clockwise in the upper/lower layers (green/red lines with arrows). (b) A thin NI layer introduces non-zero interlayer coupling, disrupting the two Majorana edge states and generating two tunable MCSs (in blue), which are driven by supercurrent (red arrow). θ_M is the angle between the line connecting two MCSs and the $+x$ axis. (c,d) Band structures of nanoribbons with x -direction periodic boundary conditions for different interlayer coupling strengths $t = 0$ in (c) and $t = 0.2$ in (d). The alternating red and blue lines represent Majorana edge states. The other parameters are set to be $m = -0.5$, $\mu = 1$, $A = 1$, $B = 1$, $\Delta = 1$, $\varphi_u = 0$, $\varphi_l = \varphi = 0$, and $N_y = 100a$.

II. MODEL AND HAMILTONIAN

We start from the QAHI-Ni-QAHI sandwich junction, which has been experimentally reported to achieve multiple chiral edge states [64]. It is worth noting that the two QAHI layers here host opposite Chern numbers, which can be achieved in a variety of ways by setting opposite magnetic orderings, applying strain, and twisting the materials, etc. [65–68]. When the intermediate NI layer is sufficiently thick, the interlayer coupling between the upper and lower QAHI layers can be ignored. In this case, we consider the simplest model Hamiltonian for upper/lower QAHI layer [69]:

$$h_{\mathbf{k}}^{u/l} = (m - Bk^2) \sigma_z \pm A\sigma_x k_x + Ak_y \sigma_y, \quad (1)$$

where $\mathbf{k} = (k_x, k_y)$ is a wave vector in the first Brillouin zone. m , A and B are material parameters, and $\sigma_{x,y,z}$ are the Pauli matrices acting on the spin space. Here, the second term in the right side of Eq. (1) is respectively $+$ and $-$ for the upper and lower QAHI layer, which corresponds to their Chern numbers being $+1$ and -1 .

In proximity to the *s*-wave SC, a finite pairing potential Δ can be induced in QAHI. The Bogoliubov-de Gennes

(BdG) Hamiltonian for the proximity-coupled QAHI is:

$$H_{\mathbf{k}}^{u/l} = \begin{pmatrix} h_{\mathbf{k}}^{u/l} + \mu & i\Delta e^{-i\varphi_{u/l}\sigma_y} \\ (i\Delta e^{-i\varphi_{u/l}\sigma_y})^\dagger & -h_{\mathbf{k}}^{u/l*} - \mu \end{pmatrix}, \quad (2)$$

where μ is the chemical potential. $\varphi_{u/l}$ is the superconducting phases of the upper/lower *s*-wave SC. The nontrivial topological phase with Chern number $\mathcal{N} = +1/\mathcal{N} = -1$ of the upper/lower layer is obtained by setting $m^2 < \Delta^2 + \mu^2$, which supports chiral Majorana edge states (MESs) propagating counterclockwise/clockwise in the upper/lower layers [34–37], as shown in Fig. 1(a).

While the intermediate NI is thin, the two converse chiral MESs are destroyed due to the introduction of interlayer coupling [see Fig. 1(b)]. Then the Hamiltonian for the SC/QAHI/Ni/QAHI/SC vertical junction is:

$$H_{\mathbf{k}} = \begin{pmatrix} H_{\mathbf{k}}^u & t\tau_0\sigma_0 \\ (t\tau_0\sigma_0)^\dagger & H_{\mathbf{k}}^l \end{pmatrix}, \quad (3)$$

where t represents the strength of the interlayer coupling, which is related to the thickness of the NI layer. τ_0 and σ_0 denote the 2×2 identity matrix acting on Nambu and spin spaces, respectively. The tight-binding form with square lattices of the above continuum model is shown in Appendix A. In our calculations, we set $A = B = 1$, $m = -0.5$ and $\Delta = 1$, which ensures that the system is in a nontrivial topological phase, as the condition $m^2 < \Delta^2 + \mu^2$ is satisfied. We focus on the effects of the superconducting phase bias, with the parameters fixed as $\varphi_u = 0$ and $\varphi_l = \varphi$. In fact, the results only depend on $\varphi_l - \varphi_u$.

III. THE REALIZATION AND MANIPULATION OF TWO MCSS

To confirm the MESs analyzed above, we plot the energy bands of the vertical junction nanoribbons with x -direction periodic boundary conditions for different interlayer coupling strengths in Figs. 1(c,d). Here, we choose the nanoribbon width to be $N_y = 100a$, where $a = 1$ is the lattice constant. Figure 1(c) shows the presence of two gapless chiral MESs in the Josephson junction with $t = 0$, corresponding to $\mathcal{N} = +1/\mathcal{N} = -1$ in the upper/lower layer. In the presence of the interlayer coupling $t = 0.2$, the MESs are gapped, as illustrated by alternating red and blue lines in Fig. 1(d).

To explore the second-order topology, we plot the energy levels for the CVJJ versus superconducting phase bias φ in Fig. 2(a). The geometry of the CVJJ is set as: we construct a square lattice plane centered at the origin $(0,0)$, where the position of each site is labeled by its coordinates (x,y) . The sites belonging to the CVJJ satisfy the condition $x^2 + y^2 < R^2$ with radius $R = 25a$. It is evident that the zero-energy in-gap states (blue lines) remain stable and separate from the other bands (black lines) throughout the variation of φ [see Fig. 2(a)]. Moreover, we plot the distribution of these in-gap states with

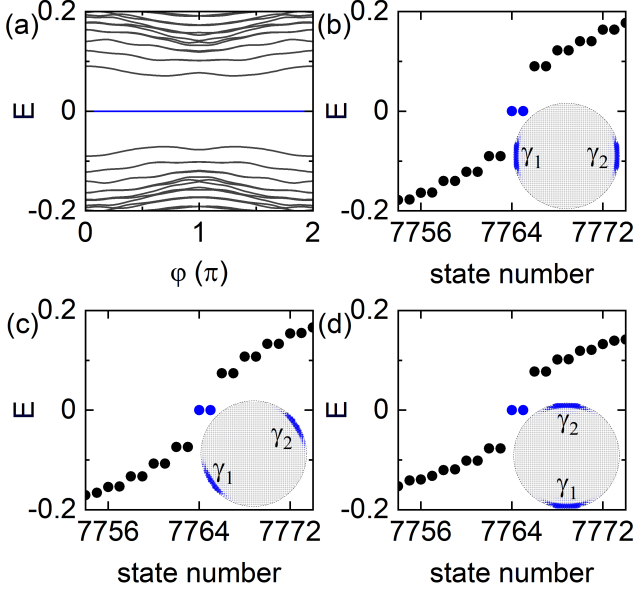


FIG. 2. (a) Band structure for the CVJJ as a function of the superconducting phase bias φ . Blue lines indicate the Majorana zero-energy bands, which always remain separate from the other bands (black lines). (b)-(d) Energy levels of the CVJJ with different superconducting phase biases $\varphi = 0$ for (b), $\varphi = 0.5\pi$ for (c) and $\varphi = \pi$ for (d). The blue dots represent the in-gap MCSs, the probability distribution of the MCSs is plotted in the inset. The radius is set to $R = 25a$ and other parameters are the same as those in Fig. 1(d).

different φ in Figs. 2(b-d). As shown in Fig. 2(b), the in-gap Majorana states localize at the left and right corners of the CVJJ with $\varphi = 0$. Figure 2(c) shows that the Majorana states are bound at the upper-right and lower-left corners of the CVJJ with $\varphi = 0.5\pi$. As the φ increases to π , the position of the MCSs shift to the upper and lower corners in Fig. 2(d). These results intuitively demonstrate that MCSs occur in the SC/QAHI/Ni/QAHI/SC vertical Josephson junction and their positions can be precisely and easily controlled by the magnitude of the superconducting phase bias φ . Furthermore, this manipulation remains robust in the elliptic vertical Josephson junctions, indicating a degree of insensitivity to geometric shape (see Appendix B).

IV. THE ORIGIN OF THE MCSS

To gain a thorough understanding of the MCSs, we analyze the chiral MESs in the s -wave SC proximity-coupled QAHI. Combining Eq. (1) with Eq. (2), the low-energy Hamiltonian can be expressed:

$$H_{\mathbf{k}}^{u/l} = (m - Bk^2)\tau_z\sigma_z \pm Ak_x\tau_0\sigma_x + Ak_y\tau_z\sigma_y + \mu\tau_z\sigma_0 - \Delta \cos \varphi_{u/l}\tau_y\sigma_y + \Delta \sin \varphi_{u/l}\tau_x\sigma_y, \quad (4)$$

where $\tau_{x,y,z}$ are the Pauli matrices acting on Nambu space. We consider a circular-shaped boundary, the nor-

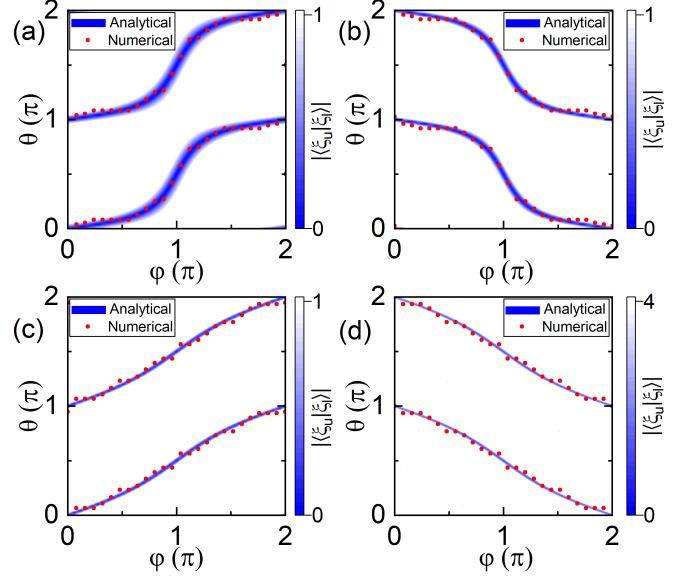


FIG. 3. The modules of the inner product of two MES spinors $|\langle \xi_u | \xi_l \rangle|$ as a function of θ and φ . The blue area corresponds to an inner product of zero, where the analytically obtained MES spinors are orthogonal. The red scatter plot numerically shows the angle θ_M at the MCSs location as a function of φ . The chemical potential is chosen as $\mu = 0.3$ in (a), $\mu = -0.3$ in (b), $\mu = 1.5$ in (c), and $\mu = -1.5$ in (d). The other parameters are the same as those in Fig. 2(b).

mal direction of the boundary tangent for arbitrary angle θ is $\hat{x}_\perp = (\cos \theta, \sin \theta)$. Next, we assume an ansatz for the edge state wave function at θ as $\Psi_{u/l}(x_\perp) = e^{\lambda x_\perp} e^{ik_\parallel x_\parallel} |\xi_{u/l}\rangle$ with $k_\parallel = \sin \theta k_x - \cos \theta k_y$. Here, $|\xi_u\rangle$ and $|\xi_l\rangle$ represent the spinor components of the chiral MESs in the upper and lower layers, respectively, and they determine whether two MESs are orthogonal. Considering a half-infinite sample area $x_\perp < 0$, we can solve out the spinors of the chiral MESs with $\varphi_u = 0$ and $\varphi_l = \varphi$:

$$|\xi_u\rangle = \begin{bmatrix} \xi_1 \\ \xi_2/[ie^{-i\theta}(\lambda - k_\parallel)] \\ \xi_3/[ie^{-i\theta}(\lambda - k_\parallel)] \\ \xi_4 \end{bmatrix}, |\xi_l\rangle = \begin{bmatrix} \xi_1 \\ \xi_2/[-ie^{i\theta}(\lambda + k_\parallel)] \\ \xi_3/[-ie^{i(\theta-\varphi)}(\lambda + k_\parallel)] \\ \xi_4/[e^{-i\varphi}] \end{bmatrix}, \quad (5)$$

where $\xi_1 = -\Delta^2 - (m + \Lambda)^2 + \mu^2 + \Lambda$, $\xi_2 = (m + \Lambda + \mu)[\Delta^2 - (m + \Lambda)^2 + \mu^2 + \Lambda]$, $\xi_3 = \Delta[-\Delta^2 + (m + \Lambda)^2 - \mu^2 + \Lambda]$, and $\xi_4 = 2\Delta(m + \Lambda + \mu)$ are the parameters shared by the two MESs. Here, $\Lambda = \lambda^2 - k_\parallel^2$ and it satisfies relationship $[-\Delta^2 + (m + \Lambda)^2 - \mu^2 - \Lambda]^2 = 4\Delta^2\Lambda$. The details for the analytic derivation are shown in Appendix C. Notably, the emergence of MCSs corresponds to the orthogonal conditions $\langle \xi_u | \xi_l \rangle = 0$ for the two MESs in the upper and lower layers [71].

In order to visualize the orthogonal position of the MESs at different superconducting phase biases, we plot the modules of the inner product of two MESs $|\langle \xi_u | \xi_l \rangle|$ as

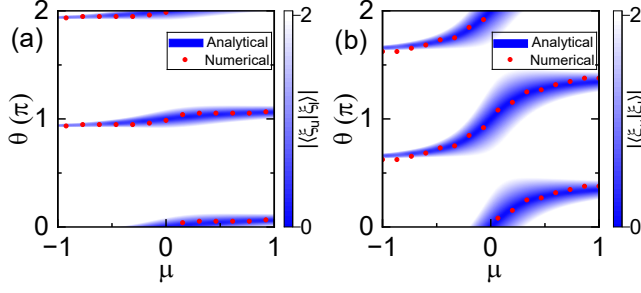


FIG. 4. The modules of the inner product of two MESs spinors $|\langle \xi_u | \xi_l \rangle|$ as a function of θ and μ . The blue area corresponds to an inner product of zero, where the analytically obtained MES spinors are orthogonal. The red scatter plot numerically shows the angle θ_M at the MCSs location as a function of the chemical potential μ . The superconducting phase bias is chosen as $\varphi = 0.2\pi$ in (a) and $\varphi = 0.8\pi$ in (b). The other parameters are set to $m = -0.5$, $A = 1$, $B = 1$, $\Delta = 1$, and $R = 25a$.

a function of θ and φ in Fig. 3. We focus on $|\langle \xi_u | \xi_l \rangle| = 0$, highlighted in blue. For $\varphi = 0$, two MESs orthogonal at $\theta = 0(2\pi)$ and $\theta = \pi$, regardless of the value of μ [see Fig. 3]. As φ changes from 0 to 2π , the values of θ corresponding to $|\langle \xi_u | \xi_l \rangle| = 0$ for the positive (negative) μ increase (decrease) from $0(\pi)$ to $\pi(0)$ and from $\pi(2\pi)$ to $2\pi(\pi)$ [Figs. 3]. For $\mu = 0.3$ and -0.3 , it changes slowly near $\varphi = 0$ and $\varphi = 2\pi$, but rapidly near $\varphi = \pi$ [see Figs. 3(a,b)]. But, for $\mu = 1.5$ and -1.5 , the process is closer to linear [see Figs. 3(c,d)]. These results show that the superconducting phase bias φ can effectively manipulate the normal angle θ that satisfies the two MESs orthogonality conditions. That is, the superconducting phase bias can effectively manipulate the position of the MCSs.

Numerically, the position of the MCSs can be labeled as θ_M . Here, $\theta_M = \pm \arctan \frac{y_2 - y_1}{x_2 - x_1}$ is defined as the angle between the lines connecting the two MCSs and the $+x$ axis [see Fig. 1(b)]. (x_1, y_1) and (x_2, y_2) are the lattice coordinates with the highest probability of MCSs. For comparison, we give the numerical results of θ_M vs φ , as represented by discrete red dots in Fig. 3. As shown in Fig. 3, the red dots are always distributed near blue area. This finding reveals that edge state orthogonality theory effectively predicts the positions of MCSs. The origin of MCSs can be understood as the fact that the MESs remain gapless at a particular angle $\theta = \theta_M$, while they are gapped at other angles $\theta \neq \theta_M$ [71].

Furthermore, we explore the role of chemical potentials in manipulating the position of the MCSs. We fix the parameters as $m = -0.5$, $\Delta = 1$. Regardless of the value of μ , the upper/lower layer remain in the nontrivial topological phase $\mathcal{N} = +1/\mathcal{N} = -1$ without interlayer coupling, as the condition $m^2 < \Delta^2 + \mu^2$ is satisfied.

In the following, we illustrate the role of the chemical potentials in manipulating the MCSs position from both edge state orthogonality analysis and numerical analysis. In Fig. 4, we plot the modules of the inner product of two

MESs spinors $|\langle \xi_u | \xi_l \rangle|$ as a function of θ and μ . We focus on $|\langle \xi_u | \xi_l \rangle| = 0$, as illustrated in blue. For $\varphi = 0.2\pi$, two MESs are orthogonal near $\theta = 0(2\pi)$ and $\theta = \pi$, regardless of the value of μ , as shown in Fig. 4(a). In this case, the effect of the chemical potential on the orthogonal angle θ between two MESs is slight. While for $\varphi = 0.8\pi$, the orthogonal angle between two MESs can be changed effectively by μ [see Fig. 4(b)]. Additionally, it changes slowly near $\mu = \pm 1$, but rapidly near $\mu = 0$. These results show that the chemical potential also plays a modulatory role in the orthogonal angles θ under a large superconducting phase bias. However, when the superconducting phase bias is small, the chemical potential does not have a significant effect on adjusting the orthogonal angle of the two MESs.

Numerically, we comparatively analyze the effect of chemical potential μ on the angle θ_M of emergence of MCSs with different superconducting phase biases in Fig. 4. As shown in Fig. 4, the discrete red dots are always distributed near blue area, which directly demonstrates the manipulating of MCSs positions by chemical potentials. This further confirms the accuracy of the edge state orthogonality theory in predicting the position of MCSs. However, substantial control of the MCSs by the chemical potential requires certain conditions, specifically that the superconducting phase bias is not very small. Even with a relatively large phase bias, simply adjusting the chemical potential is insufficient to exchange the two MCSs. In contrast, superconducting phase bias φ is more advantageous as it enables more effective and precise manipulation of the MCSs, achieving topological braiding.

V. BRAIDING BY SWAPPING TWO OF FOUR MCSS

The results above have achieved the exchange of positions between two MCSs induced by φ or μ , forming the basis for topological braiding. To further construct a qubit, it is necessary to exchange any two of the four Majorana zero modes. To achieve this, we design a hybrid system consisting of three CVJJs $\eta = I, II, III$ [see the inset in Fig. 5(b)], in which phase biases φ_η can be individually controlled. The radius of each CVJJ is set to $R = 20a$ and the center coordinates of the three CVJJs are $(0, 0)$, $(-R, -\sqrt{3}R)$ and $(R, -\sqrt{3}R)$, respectively. The Hamiltonian of the hybrid system can be written as $H_S = \sum_\eta H_\eta + H_c$. H_η is the Hamiltonian of the single junction, which can be described by Eq. (3). The coupling Hamiltonian H_c between the two CVJJs is $H_c = t_1 \rho_0 \tau_z \sigma_0$, where ρ_0 denotes the 2×2 identity matrix acting on layer degree of freedom and t_1 is the interjunction coupling strength. The corresponding tight-binding Hamiltonian of the hybrid system is provided in Appendix A.

To show the process of the topological braiding, we tune the time-dependent intensities of superconducting phase bias φ_η , as displayed in Fig. 5(a). In Figs. 5(b)-

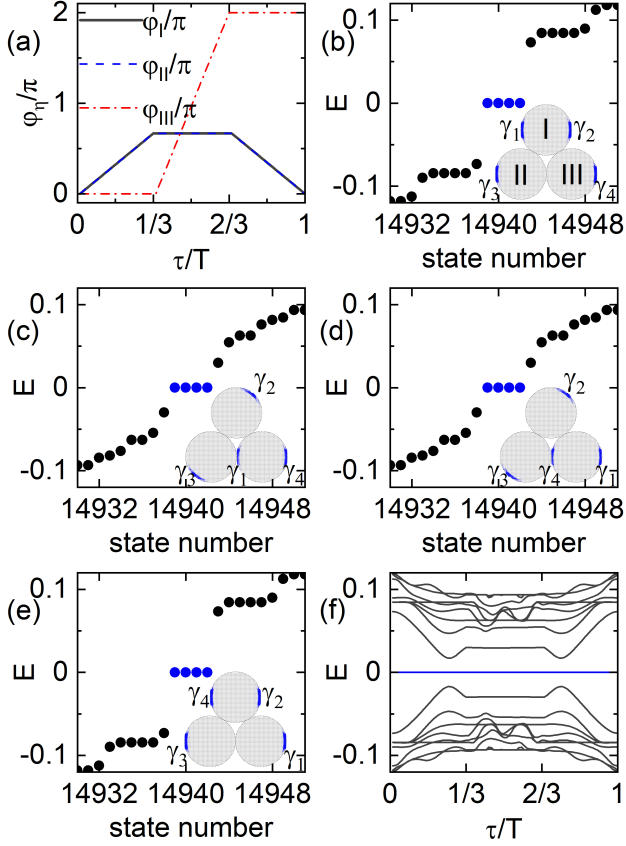


FIG. 5. (a) Superconducting phase biases $\varphi_{I,II,III}$ vs time τ in the hybrid system of three CVJJs. (b)-(e) Energy levels of the hybrid system with different time $\tau = 0$ in (b), $\tau = T/3$ in (c), $\tau = 2T/3$ in (d) and $\tau = T$ in (e). The blue dots represent the in-gap MCSs, whose probability distributions are plotted in the inset. (f) Band structure for the hybrid system as a function of time τ . Blue lines indicate the MCSs, which always remain separate from the other states (black lines). We set the parameters as $\mu = 1.5$, $R = 20a$, and $t_1 = 0.2$. Other parameters are the same as those in Fig. 2(b).

5(e), we calculate the energy levels of the hybrid system with different time τ . The braiding protocol takes four steps in T time to spatially swap two MCSs γ_1 and γ_4 : (i) At $\tau = 0$, we set $\varphi_I = \varphi_{II} = \varphi_{III} = 0$. Figure 5(b) shows that four MCSs (blue dots) are present in the three CVJJs. Specifically, γ_1, γ_2 arise at the left and right corners of CVJJ I. While γ_3 and γ_4 appear to the left of CVJJ II and to the right of CVJJ III, respectively [see the inset of Fig. 5(b)]. These four MCSs can be considered as our initial state in the topological braiding processing. (ii) At $\tau = T/3$, the superconducting phase bias change to $\varphi_I = \varphi_{II} = 2\pi/3$, $\varphi_{III} = 0$. γ_1 moves to CVJJ III, and the remaining three MCSs γ_2, γ_3 and γ_4 are located in the CVJJ I, II and III, respectively [see Fig. 5(c)]. (iii) For $\tau \in [T/3, 2T/3]$, we only increase φ_{III} from 0 to 2π , and keep the rest of the phase biases unchanged. It can be seen from Fig. 5(d) that the position of γ_2 and γ_3 remains unchanged, while the positions

of γ_1 and γ_4 are exchanged in the CVJJ III. (iv) For $\tau \in [2T/3, T]$, we leave the superconducting phase bias of CVJJ III unchanged at $\varphi_{III} = 2\pi$ and change the remaining two superconducting phase biases to $\varphi_I = 0$ and $\varphi_{II} = 0$. One can see from Fig. 5(e) that γ_4, γ_2 are bounded at the left and right corners of CVJJ I, while γ_3 and γ_1 appear to the left of CVJJ II and to the right of CVJJ III, respectively. The spatial positions of γ_1 and γ_4 are mutually swapped, and the spatial positions of γ_2 and γ_3 remain unchanged [see the inset of Figs. 5(b) and 5(e)]. In Video of the Supplementary Material [70], we show the animation of the braiding process when the time τ increases from 0 to T as shown in Fig. 5(a).

In order to observe whether the four MCSs are excited throughout the entire braiding process, we plot the energy levels of the hybrid system as a function of the time τ [see Fig. 5(f)]. One can see that the MCSs (blue lines) remain stable throughout the variation of τ . The isolated MCSs can completely prevent mixing with other states (black lines) by an energy gap. Thus, our results validate the stability of the braiding process in the hybrid system. Furthermore, any two adjacent MCSs of the four MCSs can be swapped in the hybrid system.

VI. SUMMARY

In summary, we propose a scheme for manipulating MCSs by superconducting phase bias in an SC/QAHI/Ni/QAHI/SC vertical Josephson junction. In experiment, the phase bias can be easily controlled by a supercurrent [72, 73] or a Superconducting Quantum Interference Device [74–76]. The recent development of microwave pulse generators has been designed for convenient digital control of the superconducting phase [77]. It is demonstrated that the position of MCSs in this setup can be precisely controlled by the phase bias. The origin and movement of the MCSs is effectively explained through the orthogonality of edge states. Furthermore, we propose a protocol to implement the swap of any two MCSs of four MCSs in the hybrid system consisting of three CVJJs. Importantly, MCSs remain stable throughout the braiding process. The stability and controllability of MCSs in this system have significant implications for topological quantum computing.

ACKNOWLEDGMENTS

This work was financially supported by the National Key Research and Development Program of China (Grant No. 2024YFA1409002), the National Natural Science Foundation of China (Grants No. 12447147, No. 124B2069, No. 12374034 and No. 12074097), the Natural Science Foundation of Hebei Province (Grant No. A2024205025), the Innovation Program for Quantum Science and Technology (Grant No. 2021ZD0302403), and the China Postdoctoral Science Foundation (Grant

No. 2024M760070). We also acknowledge the High-performance Computing Platform of Peking University for providing computational resources.

APPENDIX A: TIGHT-BINDING MODEL

Since the tight-binding representation is used in our calculations, the continuous Hamiltonian of the single vertical Josephson junction can be mapped onto a tight-binding representation on a two-dimensional square lattice as:

$$\begin{aligned}
 H &= \sum_{\mathbf{i}} \left[\psi_{\mathbf{i}}^\dagger T_0 \psi_{\mathbf{i}} + \left(\psi_{\mathbf{i}}^\dagger T_x \psi_{\mathbf{i}+\delta\mathbf{x}} + \psi_{\mathbf{i}}^\dagger T_y \psi_{\mathbf{i}+\delta\mathbf{y}} \right) + \text{H.c.} \right], \\
 T_0 &= (m - 4B) \rho_0 \tau_z \sigma_z + \mu \rho_0 \tau_z \sigma_y + t \rho_x \tau_0 \sigma_0 \\
 &\quad - \Delta \frac{\rho_0 + \rho_z}{2} \tau_y \sigma_y - \Delta \cos \varphi \frac{\rho_0 - \rho_z}{2} \tau_y \sigma_y \\
 &\quad + \Delta \sin \varphi \frac{\rho_0 - \rho_z}{2} \tau_x \sigma_y, \\
 T_x &= B \rho_0 \tau_0 \sigma_z + \frac{A}{2i} \rho_z \tau_0 \sigma_x, \quad T_y = B \rho_0 \tau_0 \sigma_z + \frac{A}{2i} \rho_0 \tau_z \sigma_y,
 \end{aligned} \tag{A1}$$

where the basis $\psi_{\mathbf{i}}^\dagger = (c_{\mathbf{i},\uparrow}^{u\dagger}, c_{\mathbf{i},\downarrow}^{u\dagger}, c_{\mathbf{i},\uparrow}^l, c_{\mathbf{i},\downarrow}^l, c_{\mathbf{i},\uparrow}^{l\dagger}, c_{\mathbf{i},\downarrow}^{l\dagger}, c_{\mathbf{i},\uparrow}^u, c_{\mathbf{i},\downarrow}^u)$, $c_{\mathbf{i},\uparrow/\downarrow}^{u/l\dagger}$ and $c_{\mathbf{i},\uparrow/\downarrow}^{u/l}$ are the creation and annihilation operator on site i of the upper/lower layer with spin \uparrow/\downarrow . $\mathbf{i} = (x, y)$ is the coordinates of the size with x and y being integers and $\delta\mathbf{x}$ ($\delta\mathbf{y}$) is the unit vector along the x (y) direction. ρ_0 and $\rho_{x,y,z}$ are the 2×2 unit matrix and the Pauli matrices acting on layer degree of freedom. The lattice constant has been set to $a = 1$ here.

For clarity, we choose the radius $R = 7a$ as an example to show the interjunction coupled lattice sites of the hybrid system consisting of three CVJJs in Fig. 6. The center coordinates of the three CVJJs are $O_I = (0, 0)$, $O_{II} = (-7a, -7\sqrt{3}a)$ and $O_{III} = (7a, -7\sqrt{3}a)$, respectively. We consider that interjunction coupling t_1 exists only between lattice sites at the boundaries of the CVJJs. According to the lattice positions shown in Fig. 6, the shortest lattice distance between CVJJs II and III is $d_{II,III} = 2a$, so we set that coupling t_1 occurs between lattice sites separated by a distance of $d_{II,III} = 2a$. However, the distance between CVJJs I and $II(III)$ is smaller. Here, we assume that coupling t_1 exists between lattice sites separated by a distance of $d_{I,II(III)} < \sqrt{2}a$. In fact, choosing $\sqrt{2}a$ or another value smaller than $2a$ does not affect the results. The tight-binding Hamiltonian for a single CVJJ is described by Eq. (A1), and the coupling Hamiltonian between the CVJJs is chosen as:

$$\begin{aligned}
 H_c &= t_1 \rho_0 \tau_z \sigma_0 \left(\sum_{j_I, j_{II}}^{d_{I,II} < \sqrt{2}} \psi_{j_I}^\dagger \psi_{j_{II}} + \sum_{j_I, j_{III}}^{d_{I,III} < \sqrt{2}} \psi_{j_I}^\dagger \psi_{j_{III}} \right. \\
 &\quad \left. + \sum_{j_{II}, j_{III}}^{d_{II,III} = 2} \psi_{j_{II}}^\dagger \psi_{j_{III}} \right) + \text{H.c.} \tag{A2}
 \end{aligned}$$

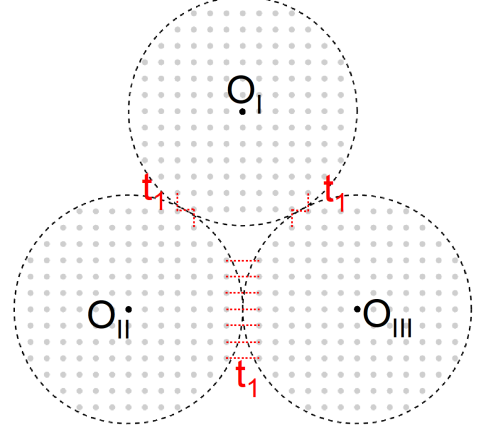


FIG. 6. Lattice configuration of the hybrid system consisting of three CVJJs. The gray dots are the lattice sites, the black dashed circles are the CVJJ boundaries, and the red dotted lines represent interjunction hopping with strength t_1 between two CVJJs. $O_I = (0, 0)$, $O_{II} = (-7a, 7\sqrt{3}a)$, and $O_{III} = (7a, 7\sqrt{3}a)$ are the coordinates of the three CVJJs' centers (black dots) with the radius $R = 7a$.

Here, the lattice distance between the lattice sites j_η of the CVJJ η and $j_{\eta'}$ of the CVJJ η' can be numerically calculated as $d_{\eta,\eta'} = \sqrt{(x_{j_\eta} - x_{j_{\eta'}})^2 + (y_{j_\eta} - y_{j_{\eta'}})^2}$.

APPENDIX B: MANIPULATING MCSS IN THE ELLIPTIC VERTICAL JOSEPHSON JUNCTIONS

To illustrate that the manipulation of MCSs is insensitive to the geometric shape of the junction, we plot the energy levels of the elliptic vertical Josephson junctions and the spatial distributions of the MCSs in Fig. 7. Specifically, the elliptic system is defined on a square lattice centered at the origin $(0, 0)$, where each lattice site is labeled by coordinates (x, y) . The sites belonging to the elliptic region satisfy the inequality:

$$\frac{(x \cos \alpha + y \sin \alpha)^2}{R_a^2} + \frac{(-x \sin \alpha + y \cos \alpha)^2}{R_b^2} < 1, \tag{B1}$$

where α is the angle between the major axis of the ellipse and the $+x$ -direction. The parameters $R_a = 27.5a$ and $R_b = 22.5a$ denote the lengths of the semi-major and semi-minor axes, respectively. In the calculations, we fix $R_a = 27.5a$, $R_b = 22.5a$, and set $\alpha = \pi/4$ in Figs. 7(a-d) and $\alpha = 3\pi/4$ in Figs. 7(e-h). All other parameters remain the same as those in Fig. 2.

Figures 7(a) and 7(e) display the energy levels of the elliptic vertical Josephson junction as a function of the superconducting phase bias φ with different angles $\alpha = \pi/4$ and $\alpha = 3\pi/4$, respectively. In both cases, the zero-energy in-gap states (blue lines) remain well separated from the other bands (black lines) throughout the full

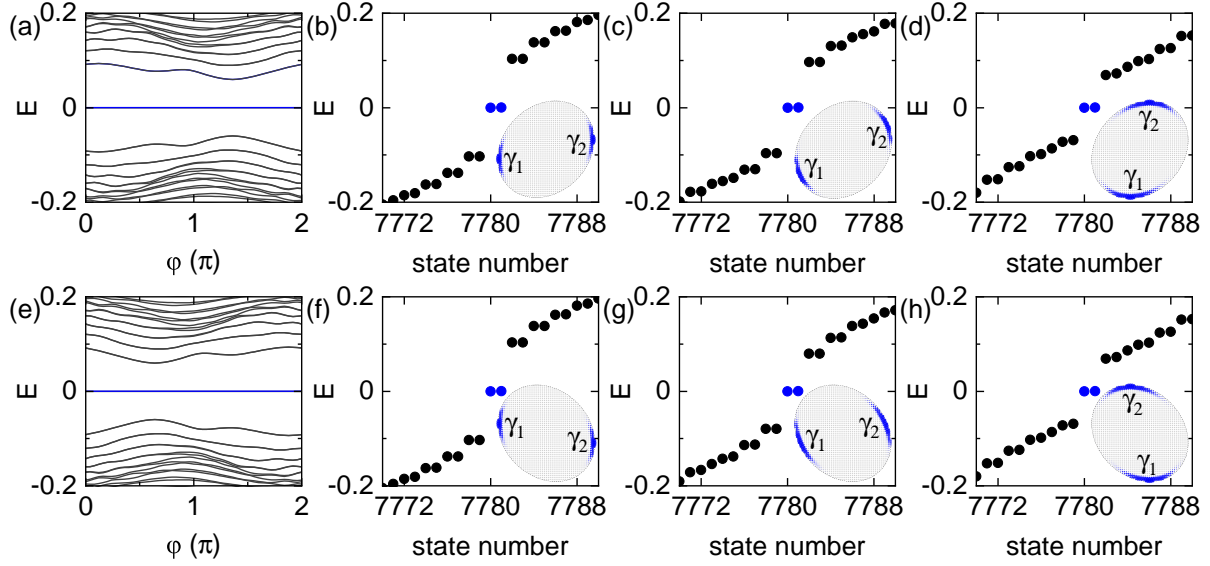


FIG. 7. (a,e) Energy spectrum of the elliptic vertical Josephson junction as a function of the superconducting phase bias φ . Blue lines represent the zero-energy Majorana bands, which always remain separate from the other bands (black lines). (b–d, f–h) Spatial probability distributions of the in-gap MCSs with different superconducting phase biases $\varphi = 0$ for (b,f), $\varphi = 0.5\pi$ for (c,g), and $\varphi = \pi$ for (d,h). The blue dots represent the in-gap MCSs, the probability distributions of the MCSs are plotted in the insets. The angle between the major axis of the ellipse and the $+x$ -direction is set to $\alpha = \pi/4$ for (a–d) and $\alpha = 3\pi/4$ for (e–h). The lengths of the semi-major axis and semi-minor axis of the ellipse are fixed as $R_a = 27.5a$ and $R_b = 22.5a$, respectively. The other parameters remain the same as those in Fig. 2

evolution of φ . This confirms that the MCSs persist and remain topologically protected even if the geometric shape of the system is elliptical with different angles.

To further explore the spatial behavior of the MCSs, we plot their probability distributions at $\varphi = 0, 0.5\pi$, and π , as shown in Figs. 7(b–d) for $\alpha = \pi/4$ and Figs. 7(f–h) for $\alpha = 3\pi/4$. In both configurations, two MCSs remain well localized at specific corners along the elliptical boundary. As the phase bias φ increases, their positions shift smoothly and predictably along the edge. Importantly, the positions of the MCSs are determined solely

by the local edge angle θ , which satisfies the edge states orthogonality condition, and are independent of the geometric shape of the junction.

These results clearly demonstrate that the phase-controlled manipulation of MCSs is robust against variations in the junction shape. The emergence and exchange of MCSs are governed by the edge angle θ , which remains fixed once the system parameters are specified. Therefore, the superconducting phase bias controlled braiding protocol proposed in the main text remains applicable even in anisotropic geometries, reinforcing the generality and flexibility of the scheme.

APPENDIX C: THE EFFECTIVE EDGE THEORY AND ORTHOGONAL CONDITIONS

We now take the lower MES as an example to derive the effective edge theory of the low-energy Hamiltonian:

$$H_{\mathbf{k}}^l = (m - B\mathbf{k}^2)\tau_z\sigma_z - Ak_x\tau_0\sigma_x + Ak_y\tau_z\sigma_y + \mu\tau_z\sigma_0 - \Delta\cos\varphi\tau_y\sigma_y + \Delta\sin\varphi\tau_x\sigma_y. \quad (\text{C1})$$

We consider a circular-shaped boundary, the normal direction of the boundary tangent for arbitrary angle θ is $\hat{x}_\perp = (\cos\theta, \sin\theta)$. Equation (C1) can be rewritten in terms of $k_x = \cos\theta k_\perp + \sin\theta k_\parallel$ and $k_y = \sin\theta k_\perp - \cos\theta k_\parallel$ as:

$$H(k_\perp, k_\parallel) = (m - Bk^2)\tau_z\sigma_z + A(-\cos\theta\tau_0\sigma_x + \sin\theta\tau_z\sigma_y)k_\perp + A(-\sin\theta\tau_0\sigma_x - \cos\theta\tau_z\sigma_y)k_\parallel + \mu\tau_z\sigma_0 - \Delta\cos\varphi\tau_y\sigma_y + \Delta\sin\varphi\tau_x\sigma_y. \quad (\text{C2})$$

To obtain the corresponding low-energy Hamiltonian which describes the MESs, we perform the replacement $k_\perp \rightarrow -i\partial_\perp$ [55–57]:

$$H(\partial_\perp, k_\parallel) = (m + B\partial_\perp^2 - Bk_\parallel^2)\tau_z\sigma_z - iA\partial_\perp(-\cos\theta\tau_0\sigma_x + \sin\theta\tau_z\sigma_y) + Ak_\parallel(-\sin\theta\tau_0\sigma_x - \cos\theta\tau_z\sigma_y) + \mu\tau_z\sigma_0 - \Delta\cos\varphi\tau_y\sigma_y + \Delta\sin\varphi\tau_x\sigma_y. \quad (\text{C3})$$

Next, we assume an ansatz for the edge state wave function at θ as $\Psi_l(x_\perp) = e^{\lambda x_\perp} e^{ik_\parallel x_\parallel} |\xi_l\rangle$. Plugging this ansatz into Eq. (C3), we obtain the eigen equation with eigenenergy $E = 0$:

$$\begin{bmatrix} (m + B\lambda^2 - Bk_\parallel^2) + \mu & iAe^{i\theta}(\lambda + k_\parallel) & 0 & \Delta e^{-i\varphi} \\ iAe^{-i\theta}(\lambda - k_\parallel) & -(m + B\lambda^2 - Bk_\parallel^2) + \mu & -\Delta e^{-i\varphi} & 0 \\ 0 & -\Delta e^{i\varphi} & -(m + B\lambda^2 - Bk_\parallel^2) - \mu & iAe^{-i\theta}(\lambda - k_\parallel) \\ \Delta e^{i\varphi} & 0 & iAe^{i\theta}(\lambda + k_\parallel) & (m + B\lambda^2 - Bk_\parallel^2) - \mu \end{bmatrix} \begin{bmatrix} \xi_a \\ \xi_b \\ \xi_c \\ \xi_d \end{bmatrix} = 0. \quad (\text{C4})$$

For simplicity, we set $A = B = 1$. A nontrivial solution of $(\xi_a, \xi_b, \xi_c, \xi_d)^T$ to Eq. (C4) yields:

$$[(m + \lambda^2 - k_\parallel^2)^2 - \Delta^2 - \mu^2 - \lambda^2 + k_\parallel^2]^2 = 4\Delta^2(\lambda^2 - k_\parallel^2). \quad (\text{C5})$$

We rewrite the above equation using $\Lambda = \lambda^2 - k_\parallel^2$ as:

$$[(m + \Lambda)^2 - \Delta^2 - \mu^2 - \Lambda]^2 = 4\Delta^2\Lambda. \quad (\text{C6})$$

Solving this, we find eight solutions of λ as $\lambda_{1/2/3/4/5/6/7/8} = \pm\sqrt{\Lambda_{1/2/3/4} + k_\parallel^2}$. Each λ corresponds to a spinor solution of $(\xi_a, \xi_b, \xi_c, \xi_d)^T$. Considering a half-infinite sample area $x_\perp < 0$ with the boundary conditions $\Psi_l(x_\perp = -\infty) = e^{\lambda(-\infty)} e^{ik_\parallel x_\parallel} \xi_l = 0$, so we keep only the four solutions with $\text{Re}[\lambda_\beta] > 0$ ($\beta = 1, 2, 3, 4$). The corresponding four spinors solutions $\xi^{\lambda_\beta} = (\xi_a^{\lambda_\beta}, \xi_b^{\lambda_\beta}, \xi_c^{\lambda_\beta}, \xi_d^{\lambda_\beta})^T$ are preserved. Assuming $\xi_a^{\lambda_\beta} = 1$, a special solution of the spinor is obtained in the form of:

$$|\xi_l\rangle = \begin{bmatrix} 1 \\ (m + \Lambda + \mu)(\Delta^2 - (m + \Lambda)^2 + \mu^2 + \Lambda)/[-ie^{i\theta}(\lambda + k_\parallel)(-\Delta^2 - (m + \Lambda)^2 + \mu^2 + \Lambda)] \\ \Delta(-\Delta^2 + (m + \Lambda)^2 - \mu^2 + \Lambda)/[-ie^{i(\theta-\varphi)}(\lambda + k_\parallel)(-\Delta^2 - (m + \Lambda)^2 + \mu^2 + \Lambda)] \\ 2\Delta(m + \Lambda + \mu)/[e^{-i\varphi}(-\Delta^2 - (m + \Lambda)^2 + \mu^2 + \Lambda)] \end{bmatrix}. \quad (\text{C7})$$

We impose the open boundary conditions $\Psi(x_\perp = 0) = e^{ik_\parallel x_\parallel} \xi = 0$ to the wave function, leading to a homogeneous linear equation $C_1\xi^{\lambda_1} + C_2\xi^{\lambda_2} + C_3\xi^{\lambda_3} + C_4\xi^{\lambda_4} = 0$, where C_1, C_2, C_3, C_4 are not all zero coefficients. The existence of such a nontrivial solution implies that the determinant $|\xi^{\lambda_1}, \xi^{\lambda_2}, \xi^{\lambda_3}, \xi^{\lambda_4}|$ equal to 0. This, together with the expressions of λ_β in Eq. (C5), we can obtain $k_\parallel = 0$. Plugging this into Eq. (C7) and simplifying gives:

$$|\xi_l\rangle = \begin{bmatrix} -\Delta^2 - (m + \Lambda)^2 + \mu^2 + \Lambda \\ (m + \Lambda + \mu)[\Delta^2 - (m + \Lambda)^2 + \mu^2 + \Lambda]/[-ie^{i\theta}(\lambda + k_\parallel)] \\ \Delta[-\Delta^2 + (m + \Lambda)^2 - \mu^2 + \Lambda]/[-ie^{i(\theta-\varphi)}(\lambda + k_\parallel)] \\ 2\Delta(m + \Lambda + \mu)/[e^{-i\varphi}] \end{bmatrix}. \quad (\text{C8})$$

Similarly, the spinor for the Chiral MES in the upper layer is:

$$|\xi_u\rangle = \begin{bmatrix} -\Delta^2 - (m + \Lambda)^2 + \mu^2 + \Lambda \\ (m + \Lambda + \mu)[\Delta^2 - (m + \Lambda)^2 + \mu^2 + \Lambda]/[ie^{-i\theta}(\lambda - k_\parallel)] \\ \Delta[-\Delta^2 + (m + \Lambda)^2 - \mu^2 + \Lambda]/[ie^{-i\theta}(\lambda - k_\parallel)] \\ 2\Delta(m + \Lambda + \mu) \end{bmatrix}. \quad (\text{C9})$$

By comparing the forms of the two spinors, we observe that they share common parameters:

$$\begin{aligned} \xi_1 &= -\Delta^2 - (m + \Lambda)^2 + \mu^2 + \Lambda, & \xi_2 &= (m + \Lambda + \mu)[\Delta^2 - (m + \Lambda)^2 + \mu^2 + \Lambda], \\ \xi_3 &= \Delta[-\Delta^2 + (m + \Lambda)^2 - \mu^2 + \Lambda], & \xi_4 &= 2\Delta(m + \Lambda + \mu). \end{aligned} \quad (\text{C10})$$

Therefore, the two spinors can be simplified as:

$$|\xi_u\rangle = \begin{bmatrix} \xi_1 \\ \xi_2/[ie^{-i\theta}(\lambda - k_{\parallel})] \\ \xi_3/[ie^{-i\theta}(\lambda - k_{\parallel})] \\ \xi_4 \end{bmatrix}, \quad |\xi_l\rangle = \begin{bmatrix} \xi_1 \\ \xi_2/[-ie^{i\theta}(\lambda + k_{\parallel})] \\ \xi_3/[-ie^{i(\theta-\varphi)}(\lambda + k_{\parallel})] \\ \xi_4/[e^{-i\varphi}] \end{bmatrix}. \quad (\text{C11})$$

It is noteworthy that the occurrence of MCSs corresponds to the orthogonal conditions $\langle \xi_u | \xi_l \rangle = 0$ of the MESs in the upper and lower layers. We analyze analytically the case where the Λ is a purely real solution, and the condition for the orthogonality of the two MESs reduces to:

$$(m + \Lambda - \mu) [1 - e^{-i(2\theta-\varphi)}] + (m + \Lambda + \mu) [-e^{-2i\theta} + e^{i\varphi}] = 0. \quad (\text{C12})$$

For $\mu = 0$, the edge states orthogonality condition reduces to

$$1 - e^{-i(2\theta-\varphi)} - e^{-2i\theta} + e^{i\varphi} = 0. \quad (\text{C13})$$

It is obvious that Eq. (C13) holds at any edge angle θ with $\varphi = \pi$. But as long as $\mu \neq 0$, $\theta = \theta_M$ satisfying the orthogonality condition can be adjusted by parameters such as the superconducting phase bias φ and chemical potential μ . The MESs of the upper and lower layers remain orthogonal only at edge $\theta = \theta_M$, which is the basis for the existence of MCSs.

-
- [1] E. Majorana, Symmetrical theory of electrons and positrons, *Nuovo Cimento* **14**, 171 (1937).
 - [2] A. Y. Kitaev, Unpaired Majorana fermions in quantum wires, *Phys. Usp.* **44**, 131 (2001).
 - [3] D. A. Ivanov, Non-Abelian Statistics of Half-Quantum Vortices in p -Wave Superconductors, *Phys. Rev. Lett.* **86**, 268 (2001).
 - [4] E. Dennis, A. Kitaev, A. Landahl, and J. Preskill, Topological quantum memory, *J. Math. Phys.* **43**, 4452 (2002).
 - [5] C. Nayak, S. H. Simon, A. Stern, M. Freedman, and S. Das Sarma, Non-Abelian anyons and topological quantum computation, *Rev. Mod. Phys.* **80**, 1083 (2008).
 - [6] J. Alicea, New directions in the pursuit of Majorana fermions in solid state systems, *Rep. Prog. Phys.* **75**, 076501 (2012).
 - [7] M. Leijnse and K. Flensberg, Introduction to topological superconductivity and Majorana fermions, *Semicond. Sci. Technol.* **27**, 124003 (2012).
 - [8] S. Nadj-Perge, I. K. Drozdov, B. A. Bernevig, and A. Yazdani, Proposal for realizing Majorana fermions in chains of magnetic atoms on a superconductor, *Phys. Rev. B* **88**, 020407(R) (2013).
 - [9] C. Beenakker, Search for Majorana Fermions in Superconductors, *Annu. Rev. Condens. Matter Phys.* **4**, 113 (2013).
 - [10] A. Yazdani, F. von Oppen, B. I. Halperin, and A. Yacoby, Hunting for Majoranas, *Science* **380**, eade0850 (2023).
 - [11] L. P. Kouwenhoven, Perspective on Majorana bound-states in hybrid superconductor-semiconductor nanowires, *Mod. Phys. Lett. B* **39**, 2540002 (2025).
 - [12] R. M. Lutchyn, J.D. Sau, and S. Das Sarma, Majorana Fermions and a Topological Phase Transition in Semiconductor-Superconductor Heterostructures, *Phys. Rev. Lett.* **105**, 077001 (2010).
 - [13] Y. Oreg, G. Refael, and F. von Oppen, Helical Liquids and Majorana Bound States in Quantum Wires, *Phys. Rev. Lett.* **105**, 177002 (2010).
 - [14] V. Mourik, K. Zuo, S. M. Frolov, S. R. Plissard, E. P. A. M. Bakkers, and L. P. Kouwenhoven, Signatures of Majorana fermions in hybrid superconductor-semiconductor nanowire devices, *Science* **336**, 1003 (2012).
 - [15] A. Das, Y. Ronen, Y. Most, Y. Oreg, M. Heiblum, and H. Shtrikman, Zero-bias peaks and splitting in an Al-InAs nanowire topological superconductor as a signature of Majorana fermions, *Nat. Phys.* **8**, 887 (2012).
 - [16] L. P. Rokhinson, X. Liu, and J. K. Furdyna, The fractional a.c. Josephson effect in a semiconductor-superconductor nanowire as a signature of Majorana particles, *Nat. Phys.* **8**, 795 (2012).
 - [17] A. D. K. Finck, D. J. V. Harlingen, P. K. Mohseni, K. Jung, and X. Li, Anomalous modulation of a zero-bias peak in a hybrid nanowire-superconductor device, *Phys. Rev. Lett.* **110**, 126406 (2013).
 - [18] H. O. H. Churchill, V. Fatemi, K. Grove-Rasmussen, M. T. Deng, P. Caroff, H. Q. Xu, and C. M. Marcus, Superconductor-nanowire devices from tunneling to the multichannel regime: Zero-bias oscillations and magnetoconductance crossover, *Phys. Rev. B* **87**, 241401(R) (2013).
 - [19] C.-M. Miao, Q.-F. Sun, and Y.-T. Zhang, Topological phase transition driven by magnetic field in one-dimensional topological superconductor rings, *Phys. Rev. B* **105**, 085401 (2022).
 - [20] X. Zhang, C.-M. Miao, Q.-F. Sun, and Y.-T. Zhang, Nonendpoint majorana bound states in an extended kitaev chain, *Phys. Rev. B* **109**, 205119 (2024).
 - [21] P. Hosur, P. Ghaemi, R. S. K. Mong, and A. Vishwanath, Majorana Modes at the Ends of Superconductor Vortices in Doped Topological Insulators, *Phys. Rev. Lett.* **107**, 097001 (2011).

- [22] G. Xu, B. Lian, P. Tang, X.-L. Qi, and S.-C. Zhang, Topological Superconductivity on the Surface of Fe-Based Superconductors, *Phys. Rev. Lett.* **117**, 047001 (2016).
- [23] Z. Wang, P. Zhang, G. Xu, L. K. Zeng, H. Miao, X. Xu, T. Qian, H. Weng, P. Richard, A. V. Fedorov, H. Ding, X. Dai, and Z. Fang, Topological nature of the $\text{FeSe}_{0.5}\text{Te}_{0.5}$ superconductor, *Phys. Rev. B* **92**, 115119 (2015).
- [24] M. Hell, M. Leijnse, and K. Flensberg, Two-Dimensional Platform for Networks of Majorana Bound States, *Phys. Rev. Lett.* **118**, 107701 (2017).
- [25] P. Zhang, K. Yaji, T. Hashimoto, Y. Ota, T. Kondo, K. Okazaki, Z. Wang, J. Wen, G. D. Gu, H. Ding, and S. Shin, Observation of topological superconductivity on the surface of an iron-based superconductor, *Science* **360**, 182 (2018).
- [26] A. Fornieri, A. M. Whiticar, F. Setiawan, E. Portolés, A. C. Drachmann, A. Keselman, S. Gronin, C. Thomas, T. Wang, R. Kallaher, G. C. Gardner, E. Berg, M. J. Manfra, A. Stern, C. M. Marcus, and F. Nichele, Evidence of topological superconductivity in planar Josephson junctions, *Nature* **569**, 89 (2019).
- [27] A. Haim and A. Stern, Benefits of weak disorder in one dimensional topological superconductors, *Phys. Rev. Lett.* **122**, 126801 (2019).
- [28] S. Hart, H. Ren, M. Kosowsky, G. Ben-Shach, P. Leubner, C. Brüne, H. Buhmann, L. W. Molenkamp, B. I. Halperin, and A. Yacoby, Controlled finite momentum pairing and spatially varying order parameter in proximitized HgTe quantum wells, *Nat. Phys.* **13**, 87 (2017).
- [29] F. Pientka, A. Keselman, E. Berg, A. Yacoby, A. Stern, and B. I. Halperin, Topological superconductivity in a planar Josephson junction, *Phys. Rev. X* **7**, 021032 (2017).
- [30] H. Ren, F. Pientka, S. Hart, A. T. Pierce, M. Kosowsky, L. Lunczer, R. Schlereth, B. Scharf, E. M. Hankiewicz, L. W. Molenkamp, B. I. Halperin, and A. Yacoby, Topological superconductivity in a phase controlled Josephson junction, *Nature* **569**, 93 (2019).
- [31] F. Setiawan, A. Stern, and E. Berg, Topological superconductivity in planar Josephson junctions: Narrowing down to the nanowire limit, *Phys. Rev. B* **99**, 220506 (2019).
- [32] A. Stern and E. Berg, Fractional Josephson vortices and braiding of Majorana zero modes in planar superconductor semiconductor heterostructures, *Phys. Rev. Lett.* **122**, 107701 (2019).
- [33] L. Fu and C. L. Kane, Superconducting Proximity Effect and Majorana Fermions at the Surface of a Topological Insulator, *Phys. Rev. Lett.* **100**, 096407 (2008).
- [34] X. L. Qi, T. L. Hughes, and S. C. Zhang, Chiral topological superconductor from the quantum Hall state, *Phys. Rev. B* **82**, 184516 (2010).
- [35] S. B. Chung, X.-L. Qi, J. Maciejko, and S.-C. Zhang, Conductance and noise signatures of Majorana backscattering, *Phys. Rev. B* **83**, 100512 (2011).
- [36] J. J. He, J. Wu, T.-P. Choy, X.-J. Liu, Y. Tanaka, and K. T. Law, Correlated spin currents generated by resonant-crossed Andreev reflections in topological superconductors, *Nat. Commun.* **5**, 3232 (2014).
- [37] Y.-T. Zhang, Z. Hou, X. C. Xie, and Q.-F. Sun, Quantum perfect crossed Andreev reflection in top-gated quantum anomalous Hall insulator-superconductor junctions, *Phys. Rev. B* **95**, 245433 (2017).
- [38] J. Alicea, Y. Oreg, G. Refael, F. von Oppen, and M. P. A. Fisher, Non-Abelian statistics and topological quantum information processing in 1D wire networks, *Nat. Phys.* **7**, 412 (2011).
- [39] T. Karzig, Y. Oreg, G. Refael, and M. H. Freedman, Universal Geometric Path to a Robust Majorana Magic Gate, *Phys. Rev. X* **6**, 031019 (2016).
- [40] Q. Yan, Y.-F. Zhou, and Q.-F. Sun, Electrically tunable chiral Majorana edge modes in quantum anomalous Hall insulator-topological superconductor systems, *Phys. Rev. B* **100**, 235407 (2019).
- [41] Y.-F. Zhou, Z. Hou, and Q.-F. Sun, Non-Abelian operation on chiral Majorana fermions by quantum dots, *Phys. Rev. B* **99**, 195137 (2019).
- [42] T. Hodge, E. Mascot, D. Crawford, and S. Rachel, Characterizing Dynamic Hybridization of Majorana Zero Modes for Universal Quantum Computing, *Phys. Rev. Lett.* **134**, 096601 (2025).
- [43] Z.-H. Wang, E. V. Castro, and H.-Q. Lin, Strain manipulation of Majorana fermions in graphene armchair nanoribbons, *Phys. Rev. B* **97**, 041414(R) (2018).
- [44] M. Li, G. Li, L. Cao, X. Zhou, X. Wang, C. Jin, C.-K. Chiu, S. J. Pennycook, Z. Wang, and H.-J. Gao, Ordered and tunable Majorana-zero mode lattice in naturally strained LiFeAs , *Nature* **606**, 890 (2022).
- [45] T. Posske, C.-K. Chiu, and M. Thorwart, Vortex Majorana braiding in a finite time, *Phys. Rev. Res.* **2**, 023205 (2020).
- [46] X. Ma, C. J. O. Reichhardt, and C. Reichhardt, Braiding Majorana fermions and creating quantum logic gates with vortices on a periodic pinning structure, *Phys. Rev. B* **101**, 024514 (2020).
- [47] T. Liu, J. J. He, and F. Nori, Majorana corner states in a two-dimensional magnetic topological insulator on a high-temperature superconductor, *Phys. Rev. B* **98**, 245413 (2018).
- [48] Q. Wang, C.-C. Liu, Y.-M. Lu, and F. Zhang, High-Temperature Majorana Corner States, *Phys. Rev. Lett.* **121**, 186801 (2018).
- [49] Z. Yan, F. Song, and Z. Wang, Majorana Corner Modes in a High-Temperature Platform, *Phys. Rev. Lett.* **121**, 096803 (2018).
- [50] X. Zhu, Tunable Majorana corner states in a two-dimensional second-order topological superconductor induced by magnetic fields, *Phys. Rev. B* **97**, 205134 (2018).
- [51] X. Zhu, Second-Order Topological Superconductors with Mixed Pairing, *Phys. Rev. Lett.* **122**, 236401 (2019).
- [52] Z. Yan, Majorana corner and hinge modes in second-order topological insulator/superconductor heterostructures, *Phys. Rev. B* **100**, 205406 (2019).
- [53] K. Laubscher, D. Chughtai, D. Loss, and J. Klinovaja, Kramers pairs of Majorana corner states in a topological insulator bilayer, *Phys. Rev. B* **102**, 195401 (2020).
- [54] Y.-J. Wu, J. Hou, Y.-M. Li, X.-W. Luo, X. Shi, and C. Zhang, In-Plane Zeeman-Field-Induced Majorana Corner and Hinge Modes in an s-Wave Superconductor Heterostructure, *Phys. Rev. Lett.* **124**, 227001 (2020).
- [55] Y. Tan, Z.-H. Huang, and X.-J. Liu, Two-particle Berry phase mechanism for Dirac and Majorana Kramers pairs of corner modes, *Phys. Rev. B* **105**, L041105 (2022).
- [56] X.-H. Pan, L. Chen, D. E. Liu, F.-C. Zhang, and X. Liu, Majorana Zero Modes Induced by the Meissner Effect at Small Magnetic Field, *Phys. Rev. Lett.* **132**, 036602 (2024).

- (2024).
- [57] S.-B. Zhang, W. B. Rui, A. Calzona, S.-J. Choi, A. P. Schnyder, and B. Trauzettel, Topological and holonomic quantum computation based on second-order topological superconductors, *Phys. Rev. Res.* **2**, 043025 (2020).
 - [58] T. E. Pahomi, M. Sigrist, and A. A. Soluyanov, Braiding Majorana corner modes in a second-order topological superconductor, *Phys. Rev. Res.* **2**, 032068(R) (2024).
 - [59] S. Ikegaya, W. B. Rui, D. Manske, and A. P. Schnyder, Tunable Majorana corner modes in noncentrosymmetric superconductors: Tunneling spectroscopy and edge imperfections, *Phys. Rev. Res.* **3**, 023007 (2021).
 - [60] L. Liu, C. Miao, H. Tang, Y.-T. Zhang, and Z. Qiao, Magnetically controlled topological braiding with Majorana corner states in second-order topological superconductors, *Phys. Rev. B* **109**, 115413 (2024).
 - [61] M. F. Lapa, M. Cheng, and Y. Wang, Symmetry-protected gates of Majorana qubits in a high- T_c higher-order topological superconductor platform, *SciPost Phys.* **11**, 086 (2021).
 - [62] M. Ezawa, Braiding of Majorana-like corner states in electric circuits and its non-Hermitian generalization, *Phys. Rev. B* **100**, 045407 (2019).
 - [63] S.-B. Zhang, A. Calzona, and B. Trauzettel, All-electrically tunable networks of Majorana bound states, *Phys. Rev. B* **102**, 100503 (2020).
 - [64] Y.-F. Zhao, R. Zhang, R. Mei, L.-J. Zhou, H. Yi, Y.-Q. Zhang, J. Yu, R. Xiao, K. Wang, N. Samarth, M. H. W. Chan, C.-X. Liu, and C.-Z. Chang, Tuning the Chern number in quantum anomalous Hall insulators, *Nature* **588**, 419 (2020).
 - [65] Z. Xu, W. Duan, and Y. Xu, Controllable Chirality and Band Gap of Quantum Anomalous Hall Insulators, *Nano Lett.* **23**, 305 (2023).
 - [66] P.-J. Guo, Z.-X. Liu, and Z.-Y. Lu, Quantum anomalous hall effect in collinear antiferromagnetism, *npj Comput. Mater.* **9**, 70 (2023).
 - [67] F. Xue, Y. Hou, Z. Wang, Z. Xu, K. He, R. Wu, Y. Xu, and W. Duan, Tunable quantum anomalous Hall effects in ferromagnetic van der Waals heterostructures, *Natl. Sci. Rev.* **11**, nwad151 (2024).
 - [68] Z. Li, J. Zhang, X. Hong, X. Feng, and K. He, Multi-mechanism quantum anomalous Hall and Chern number tunable states in germanene (silicene, stanene)/ MBi_2Te_4 heterostructures, *Phys. Rev. B* **109**, 235132 (2024).
 - [69] X.-L. Qi, Y.-S. Wu, and S.-C. Zhang, Topological quantization of the spin Hall effect in two-dimensional paramagnetic semiconductors, *Phys. Rev. B* **74**, 085308 (2006).
 - [70] See Supplemental Material at [url] for Video of the entire braiding process.
 - [71] C.-M. Miao, Y.-H. Wan, Y.-T. Zhang, Q.-F. Sun, Tunable second-order topological corner states induced by interlayer coupling in twisted bilayer Chern insulators, *Phys. Rev. B* **111**, 165418 (2025).
 - [72] A. Melo, S. Rubbert, and A. R. Akhmerov, Topological quantization of the spin Hall effect in two-dimensional paramagnetic semiconductors, *SciPost Phys.* **7**, 039 (2019).
 - [73] O. Lesser, A. Saydjari, M. Wesson, A. Yacoby, and Y. Oreg, Phase-induced topological superconductivity in a planar heterostructure, *Proc. Natl. Acad. Sci. USA* **118**, e2107377118 (2021).
 - [74] R. L. Fagaly, Superconducting quantum interference device instruments and applications, *Rev. Sci. Instrum.* **77**, 101101 (2006).
 - [75] F. Giazotto, J. T. Peltonen, M. Meschke, and J. P. Pekola, Superconducting quantum interference proximity transistor, *Nat. Phys.* **6**, 254 (2010).
 - [76] T. Noh, A. Kindseth, and V. Chandrasekhar, Nonlocal superconducting quantum interference device, *Phys. Rev. B* **104**, 064503 (2021).
 - [77] Z. Bao, Y. Li, Z. Wang, J. Wang, J. Yang, H. Xiong, Y. Song, Y. Wu, H. Zhang, and L. Duan, A cryogenic on-chip microwave pulse generator for large-scale superconducting quantum computing, *Nat. Commun.* **15**, 5958 (2024).